Supporting Information

Mesoporous Carbon Encapsulated Zinc Oxide Nanorods Derived from Plant Species 'Argyreia sharadchandrajii' for Live Cell Imaging of Drug Delivery and Multimodal Bioactivities

Sneha R. Bhosale[a], Kishor S. Jagadhane[a], Rakhee R. Bhosale[b], Sharadrao A. Vanalakar[c,d], Mohammad H. Qureshi[d], Devashree N. Patil[e], Rushikesh P. Dhavale[f], Vinod B. Shimpale[g], Govind B. Kolekar[h], Prashant V. Anbhule[a*]

[a]Medicinal Chemistry Research Laboratory, Department of Chemistry, Shivaji University Kolhapur, India-416004

[b]Analytical Chemistry and Material Science Research Laboratory, Department of Chemistry, Shivaji University Kolhapur, India-416004

[c]Department of Physics, Karmaveer Hire College, Gargoti, India-416209

[d]Translational Medicine Research Centre, KOC University, Sariyer, Istanbul Turkey-34450

[e]Department of Biotechnology, Shivaji University Kolhapur, India-416004

[f]Department of Materials Science and Engineering, Yonsei University, Seoul, South Korea-03722,

[g]Department of Botany, The New College Kolhapur, India-416012

[h]Fluorescence Spectroscopy Research Laboratory, Department of Chemistry, Shivaji University, Kolhapur 416004, India

Keywords: Bioderived Mesoporous Carbon; Nanorods; Antimicrobial; Anticancer; Drug Delivery; Live Imaging;

***Corresponding Author:** Prof. (Dr.) Prashant V. Anbhule

Email: pva_chem@unishivaji.ac.in

S1. Raman analysis of bioderived carbon samples

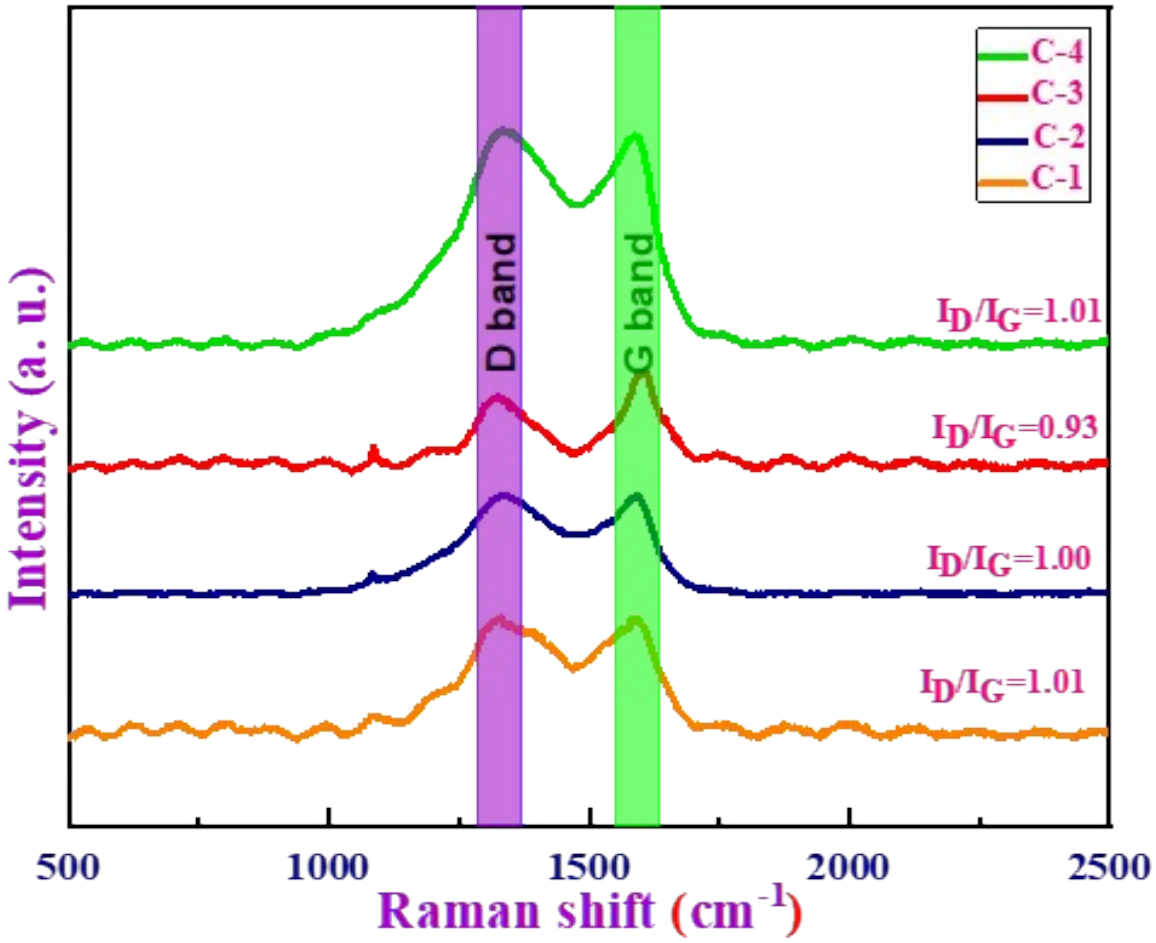

Fig. S1 Raman spectra of bioderived carbon samples (C-1, C-2, C-3 and C-4)

Raman spectroscopy is used to resolve the graphitization degree, which is a key factor in determining the electrical properties of carbon materials. As per literature, the Raman spectra indicate the degree of graphitization (I_D/I_G) is the peak intensity ratio of the D-band and G-band of carbon materials. The D-band intensity designates the number of defects in the carbon material, which are treated as an active site for the adsorption phenomenon and resemble sp^3 hybridization. The G-band, on the other hand, corresponds to sp^2 hybridization, thereby exhibiting the carbon materials graphitic properties that are advantageous for improving its electrical conductivity. Fig. S1. reveals the ratio of I_D/I_G for C-1, C-2, C-3, and C-4 are 1.01, 1.00, 0.93, and 1.01 respectively, which suggests the amorphous nature of synthesized carbon material. As amorphous carbon does not have the same electrical conductivity as graphitic

carbon, it is considerably easier for amorphous carbon materials to acquire a large surface area. The I_D/I_G value for C-3 is the smallest among the rest of the samples and offers fewer active sites but perhaps strong electrical conductivity. The highest I_D/I_G values were found for the C-1 and C-4 samples representing a higher number of active sites and probably lower electrical conductivity.The I_D/I_G value of the C-2 was balanced, indicating an equilibrium between active site quantities and electrical conductivity for offering enough active sites for the adsorption of ions[1].

S2. Phase identification and crystallinity of ZnO samples

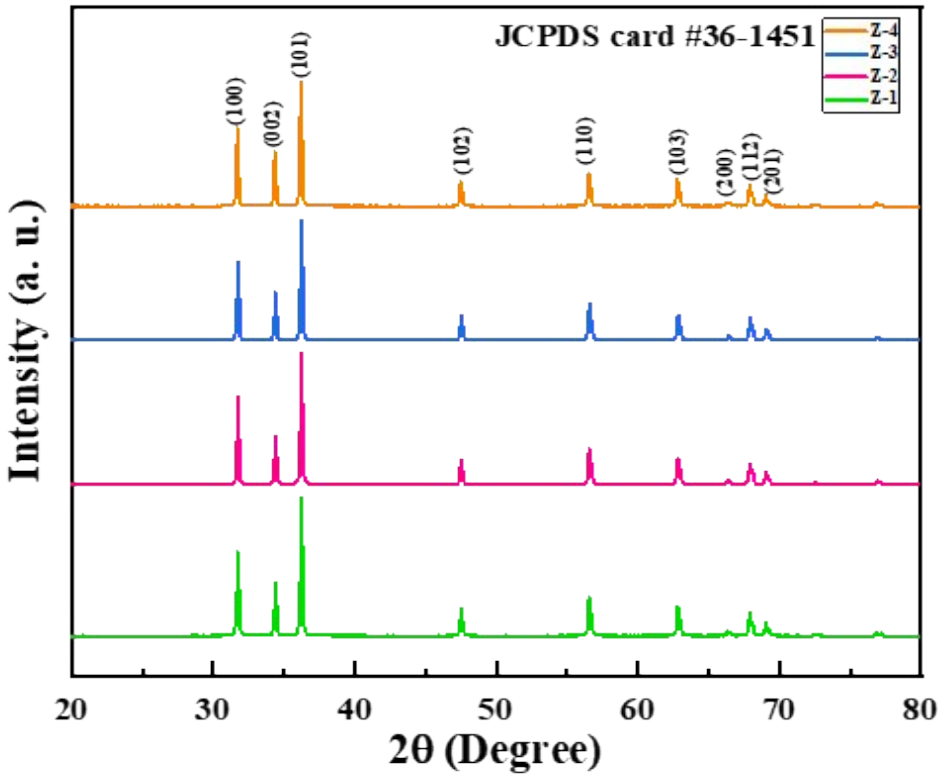

Fig. S2 XRD spectra of hydrothermally prepared ZnO samples (Z-1, Z-2, Z-3 and Z-4)

The crystallinity and structural orientations of the synthesized ZnO nanostructures were probed with XRD analysis. The nanostructures of ZnO were investigated through a range of 2θ = 20-80°.Fig. S2 illustrates the diffractograms of ZnO nanostructures manufactured by the hydrothermal strategy for 3 h at 90 °C with and without the aid of surfactants denoted as Z-1, Z-2, Z-3, and Z-4 respectively. No other peaks of impurities were revealed in the diffraction patterns of ZnO. The diffraction peaks at angle 2θ ~ 31.7, 34.4, 36.1, 47.5, 56.4, 62.7, 66.4, 67.8, 69.0 correspond to planes (100), (002), (101), (102), (110), (103), (200), (112), and (201) and can be indexed as wurtzite hexagonal crystal structure and well matched with JCPDS card no. 36-1451[2–4].

The average crystallite size for different samples of ZnO nanostructures was estimated by using the Debye Scherrer equation as shown below,

$$D = \frac{K\lambda}{\beta Cos\theta} \text{.....(1)}$$

Where, 'β' is full width at half maximum (FWHM) in radians of the diffraction peak 2θ, 'λ' is wavelength = 1.54 Å (Cu-Kα), and 'θ' is the Bragg's angle. The calculated crystallite size of the ZnO samples was in the range of 47.04 - 58.19 nm. The smallest crystallite size was found for Z-2 accompanied by Z-4, Z-3, and Z-2 respectively which builds them as a favorite contender for biomedical applications.

S3. Functional moieties and chemical structure of carbon and ZnO samples

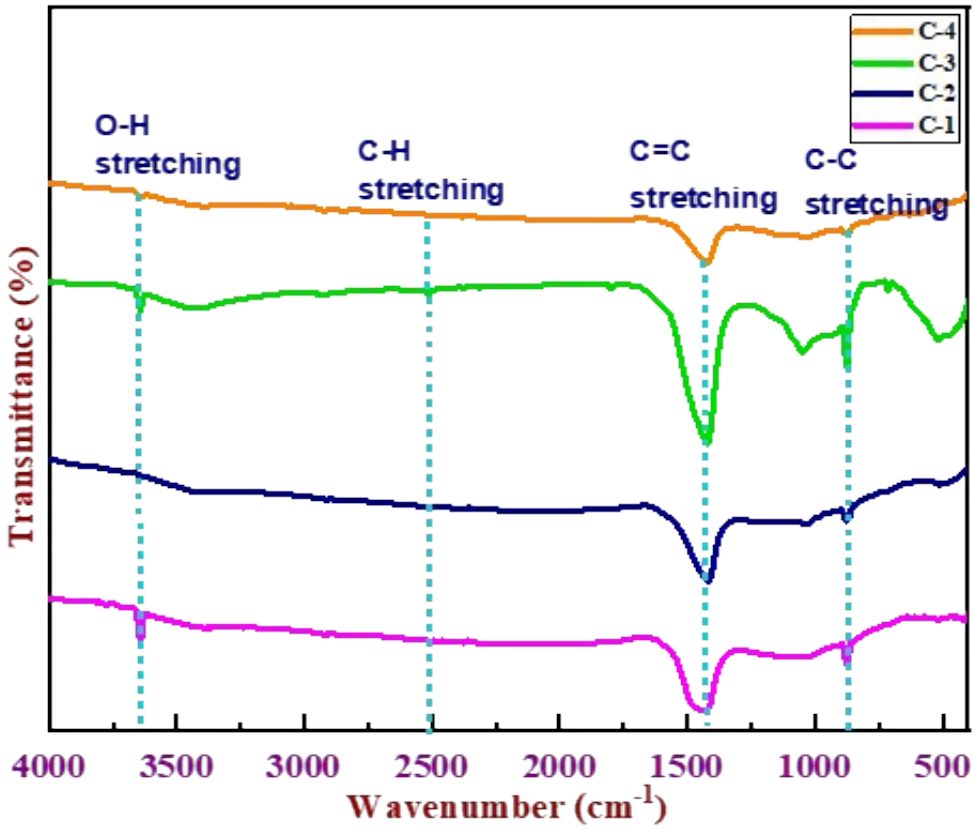

Fig. S3 (a) FT-IR spectra of carbon samples (C-1, C-2, C-3 and C-4)

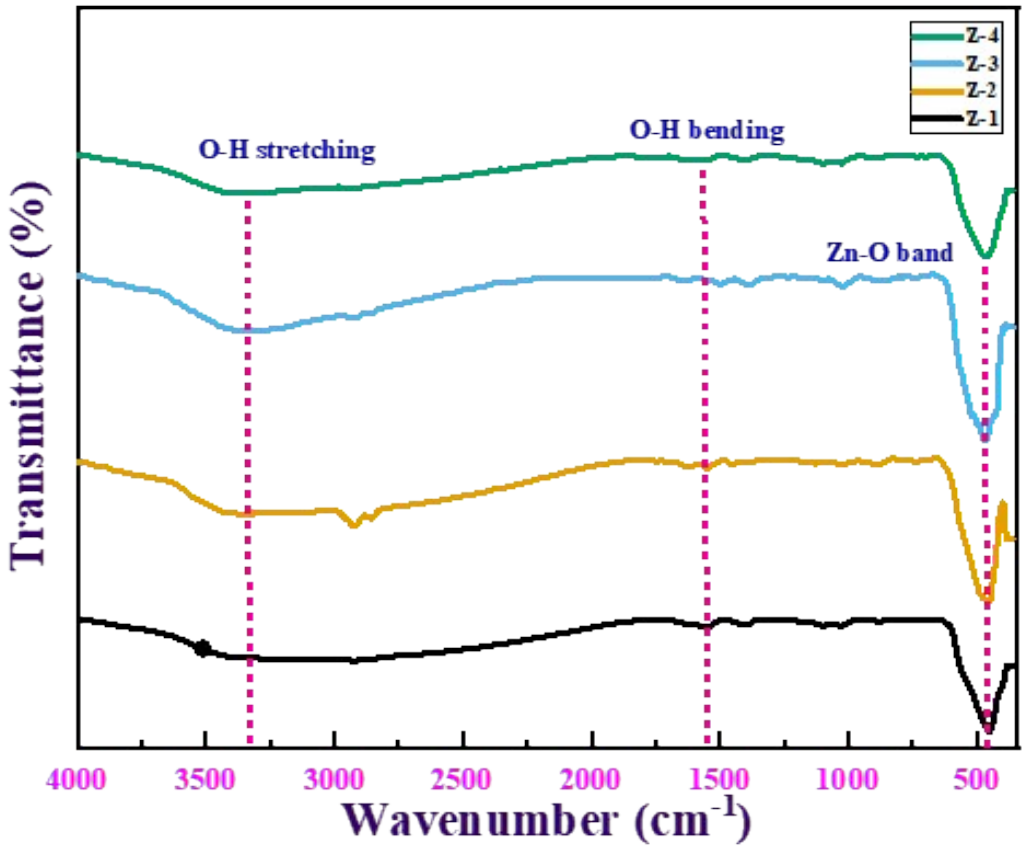

Fig. S3(b) FT-IR spectra of ZnO samples (Z-1, Z-2, Z-3 and Z-4)

A Fourier transform infrared spectroscopy (FT-IR) technique reviews ideas regarding surface functionalities and chemical structure of the bioderived carbon samples as shown in Fig. S3 (a). The intense vibrational bands of O-H, C-H, and C=C are observed in all four variations of carbon samples C-1, C-2, C-3, and C-4. The band at 3642 cm^{-1} is assigned to the O-H stretching vibrations of a hydroxyl group of the adsorbed water molecules on the carbon material probably while handling the sample to scan the FT-IR spectrum. The weak band at 2500 cm^{-1} exhibits the C-H asymmetric vibrations of hydrocarbon groups. The band at 1472 cm^{-1} can be attributed to C=C stretching vibrations. The appearance of broad band around 1500 cm^{-1} in the FT-IR spectra shows a high degree of aromatization in the carbon samples due to the presence of larger aromatic moieties (C=C) in the carbon structure. The bands detected between 1100 cm^{-1} and 400 cm^{-1} may be ascribed to the C-C, C-N, and C-O stretching. The weak band around 2500 cm^{-1} in

the spectrum is due to the carbonization of bioderived carbon materials at high temperatures lead to the evaporation of volatile compounds results collapsing of the carbon framework. Similarly, Fig. S3 (b) shows the FT-IR spectra of pure ZnO and surfactant modified ZnO nanostructures. The sharp absorption band detected in the region from 450 cm^{-1} to 520 cm^{-1} resembles the standard characteristic band of ZnO due to the Zn-O stretching vibrations of ZnO nanostructures. The intense absorption band of Zn-O stretching vibrations was observed in the Z-3 sample followed by Z-2, Z-1, and Z-4 respectively. However, in FT-IR spectra the less intense peaks observed around 1500 cm^{-1} to 1650 cm^{-1} in our study belong to H-O-H bond vibrations.

S4. Elemental composition and chemical study of C-2 and Z-2 samples

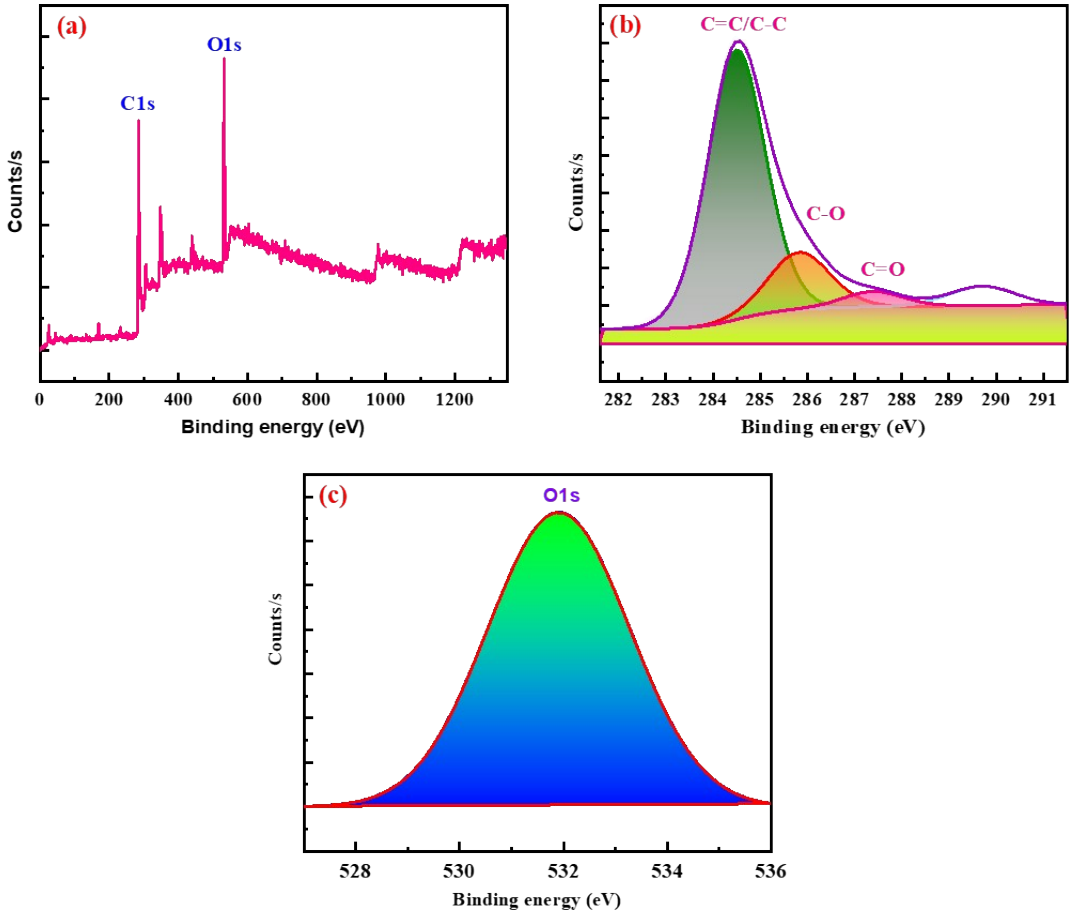

Fig. S4(A) XPS spectrum of C-2 sample, (a) Survey scan spectra of C-2 sample (b) Narrow scan spectra of 'C' element (c) Narrow scan spectra of 'O' element

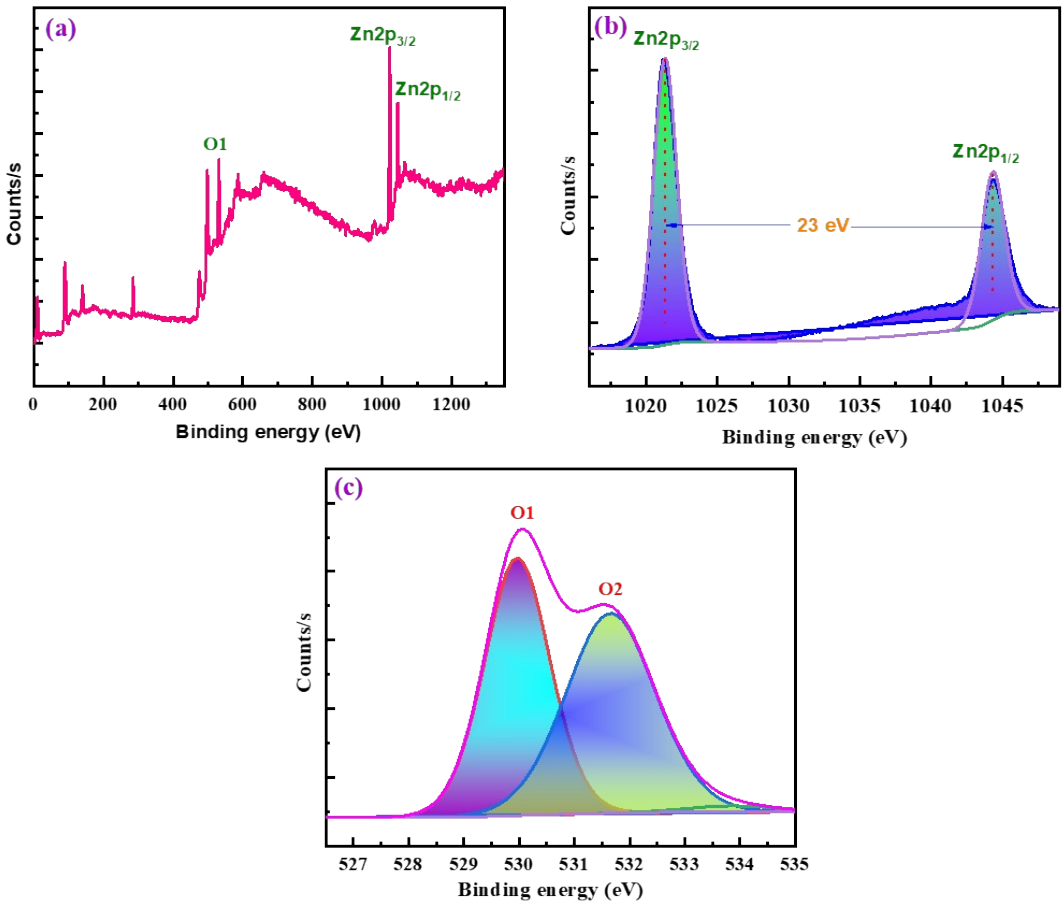

Fig. S4 (B) XPS spectrum of Z-2 sample, (a) Survey scan spectra of Z-2 sample (b) Narrow scan spectra of 'Zn' element (c) Narrow scan spectra of 'O' element

X-ray Photoelectron Spectroscopy (XPS) was used to determine the chemical composition of samples of C-2 and Z-2, as shown in Fig. S4 (a) and (b). The C-2 sample's XPS spectra is shown in Fig S4 (a) while the Fig. S4 (b) represents XPS spectra of Z-2 sample.

S5. Surface morphological study of all carbon and ZnO samples

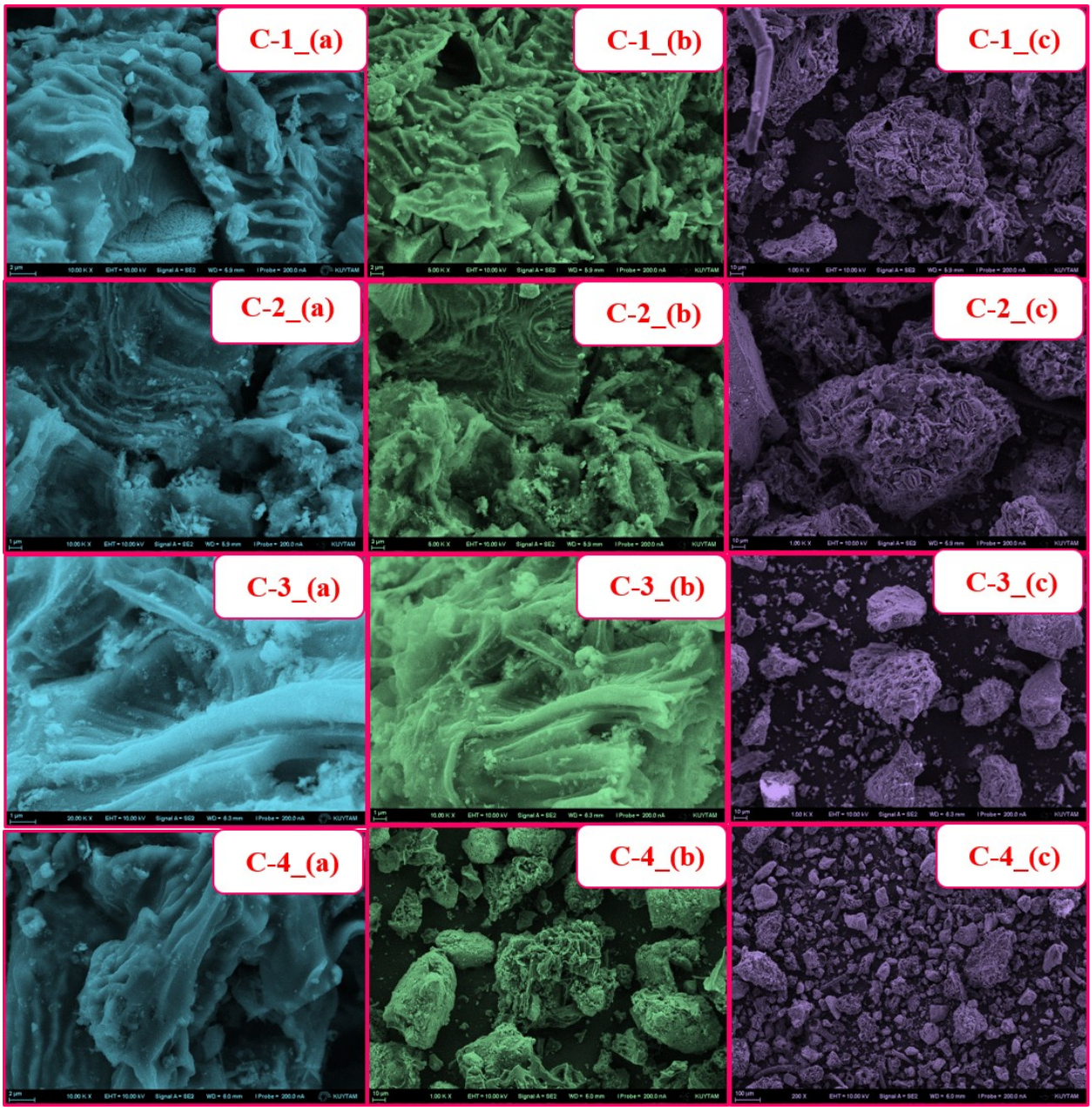

Fig. S5 (a) SEM images of carbon samples (C-1, C-2, C-3 and C-4)

The surface morphologies of bioderived carbon (C-1, C-2, C-3 and C-4) and surfactants-assisted ZnO samples (Z-1, Z-2, Z-3 and Z-4) with different magnifications were examined by usingthe SEM technique. The carbon prepared from Argyreia Sharadchandrajii (A. S.) plant employing different surfactants exhibited distinct morphologies as shown inFig. S5 (a). The

sheets-like morphology with pores on the surface of the C-1 sample was observed. As the surfactants changes, there is a change in the morphology with mesoporous structure. Also, as the change in a surfactant, two-dimensional sheets like morphology appeared. Among all these samples C-2 shows a highly porous structure with some voids. Hence, it will be beneficial for biomedical applications.

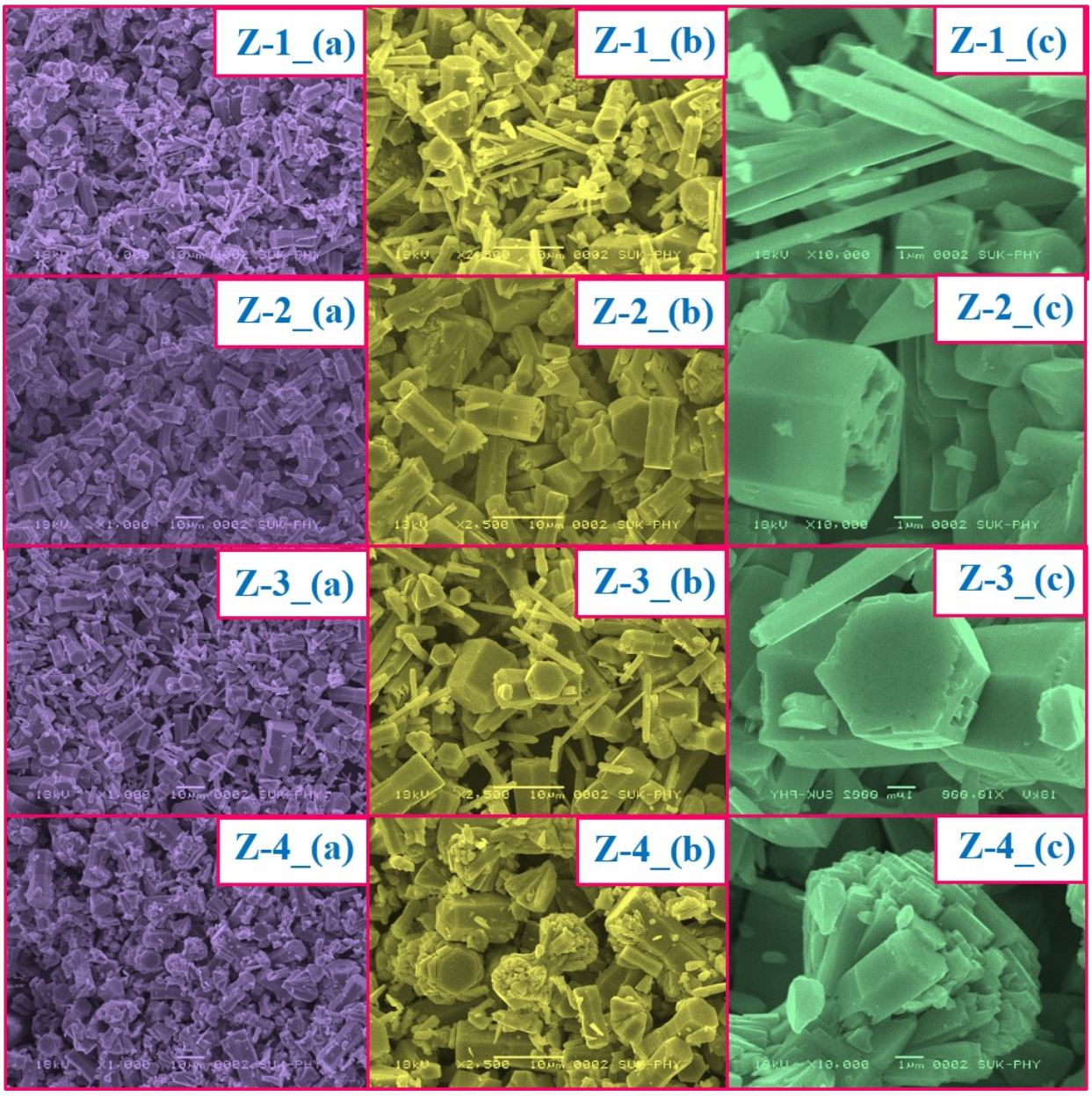

Fig. S5 (b) SEM images of ZnO samples (Z-1, Z-2, Z-3 and Z-4)

Again, Fig. S5 (b) shows the SEM images of zinc oxide nanostructures synthesized by the hydrothermal method. It showed the one-dimensional rod-like morphology was observed in all the ZnO samples. As a change in the surfactants, there is a change in the aspect ratio of the nanorods was witnessed in all the samples. The image depicts that the use of different surfactants offers different morphology from elongated nanorods to shorten nanorods. The variation detected in the ZnO nanostructures was surfactant-dependent. In Z-1_(c) the rods were elongated and thin compared to other surfactant-boosted samples. With the use of surfactant CTAB in Z-2_(c) the rods get shortened with an increase in breadth of rods, the same followed in Z-3_(c) sample of PVP-assisted ZnO. In Z-4_(c), the PEG-assisted ZnO samples the rods get agglomerated with a decrease in the size of rods with an increased breadth, which outcomes in the increase in surface area of rods. Among all the samples, Z-2 presented a long length with a diameter of a few nanometers in size and was randomly oriented with uniform dimensions all over the sample. Hence, increases the surface area of the sample which will be helpful in the enhancement of the biomedical application.

S6. BET analysis of all carbon and ZnO samples

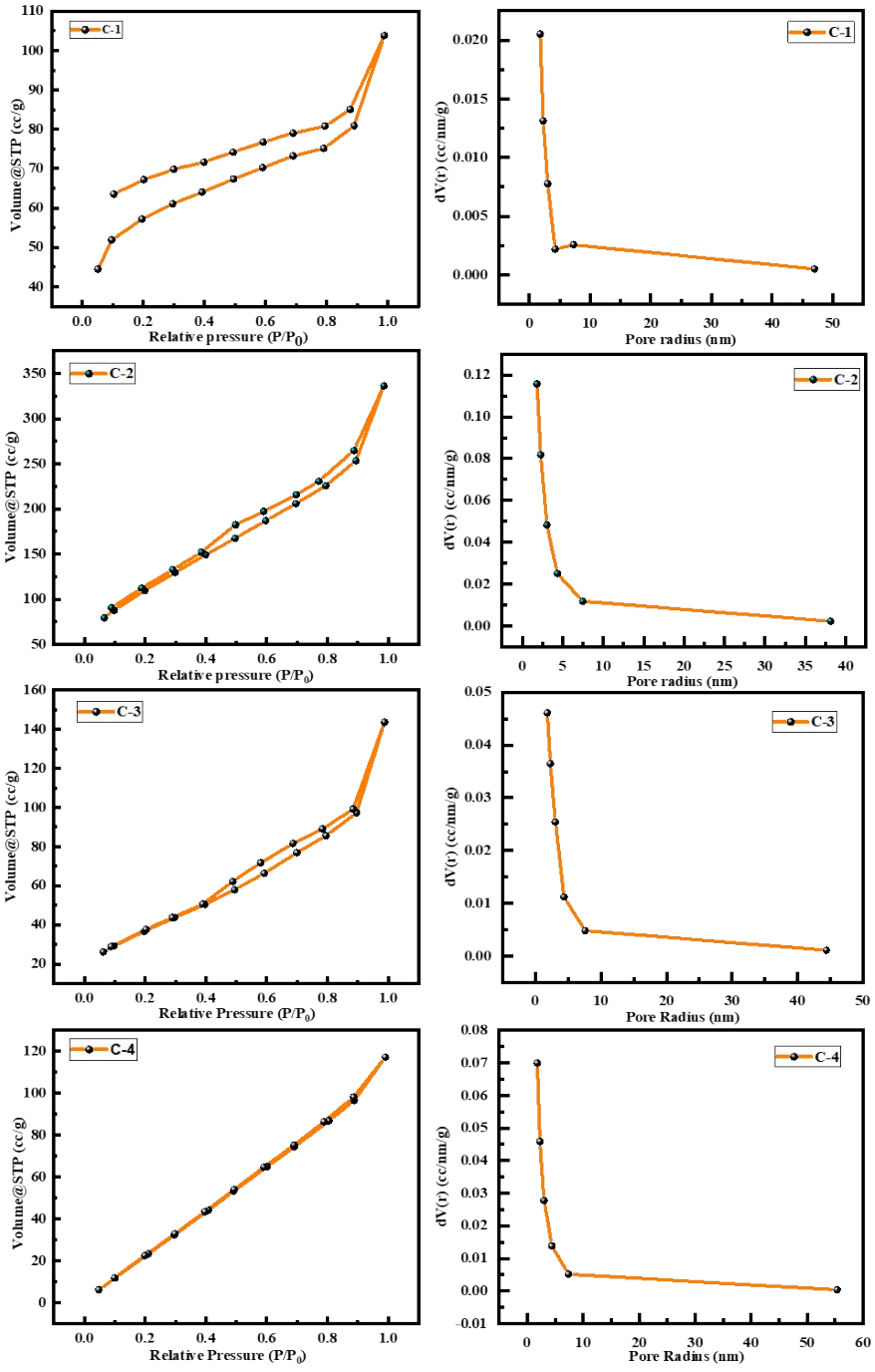

Fig. S6 (a) Nitrogen adsorption-desorption isotherms and pore size distribution graphs of carbon samples (C-1, C-2, C-3 and C-4)

BET analysis was performed to study the textural characteristics like specific surface area (SSA) and porosity of bioderived carbon. The SSA is one of the crucial aspects of the carbon material for assessing it as an adsorbent material in biomedical applications. Fig. S6 (a) reveals the N_2 adsorption-desorption isotherms of pure bioderived carbon material with three different surfactant assistant carbon contents designated as C-1, C-2, C-3, and C-4. In accordance with the IUPAC (1985) nomenclature the typical type II and IV, isotherm curves as manifested in Fig. S6 (a) resemble the presence of mesoporous structures[5,6].With the variation of carbon content, the BET SSA of carbon material increased from 136.95 m^2/g of C-3 carbon sample to 171.22 m^2/g (C-4), 189.33 m^2/g (C-1), and 409.61 m^2/g (C-2) respectively. The extortionate SSA correlates to the high adsorption properties of the carbon material[7].Amongst all C-2 exhibits a high SSA which shows outstanding results in biomedical applications. Additionally, the average pore size distribution of C-1, C-2, C-3, and C-4 samples are 16.67 nm, 14.29 nm, 16.85 nm, and 19.14 nm respectively, which confirms the mesoporous nature of carbon as the average pore size lies below the 50 nm. Our affirmed results are in excellent compliance with the above assumptions as the SSA increases particle size decreases and the adsorption properties increase which outcomes great antioxidant activity, antimicrobial activity, anticancer activity as well as drug loading and release study in our case of biomedical applications.

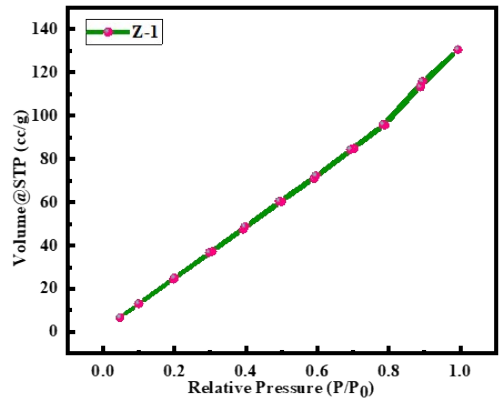
Z-1
Volume@STP (cc/g)
Relative Pressure (P/P0)

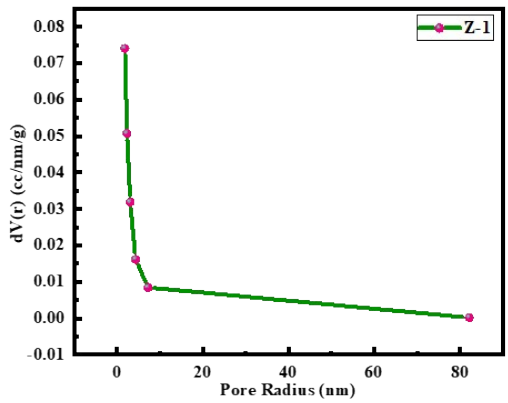
Z-1
dV(r) (cc/nm/g)
Pore Radius (nm)

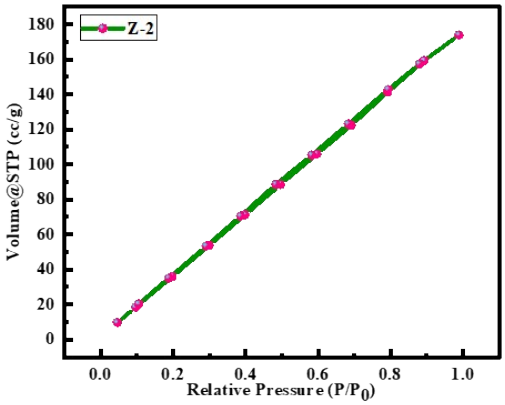
Z-2
Volume@STP (cc/g)
Relative Pressure (P/P0)

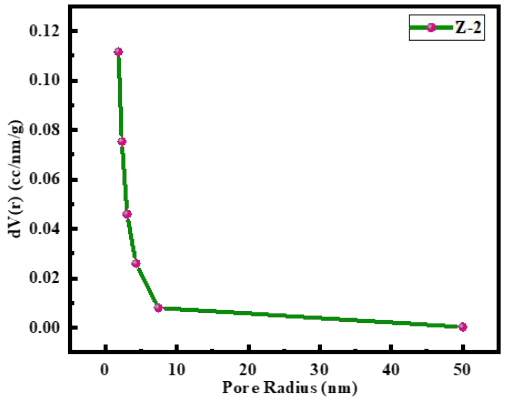
Z-2
dV(r) (cc/nm/g)
Pore Radius (nm)

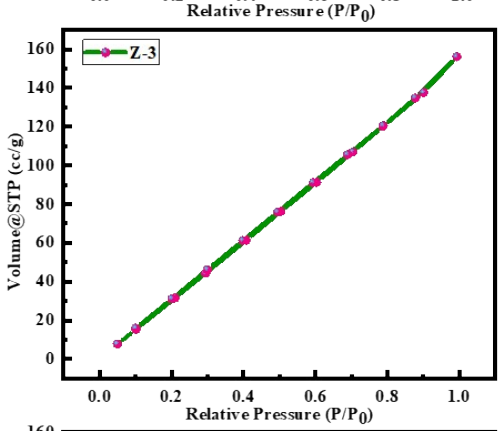
Z-3
Volume@STP (cc/g)
Relative Pressure (P/P0)

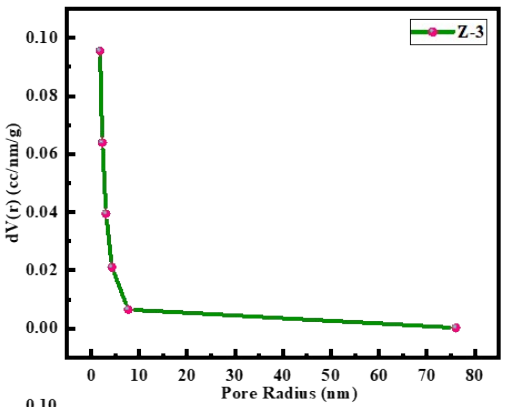
Z-3
dV(r) (cc/nm/g)
Pore Radius (nm)

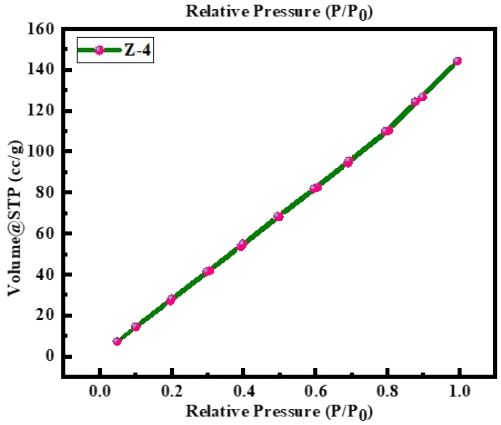
Z-4
Volume@STP (cc/g)
Relative Pressure (P/P0)

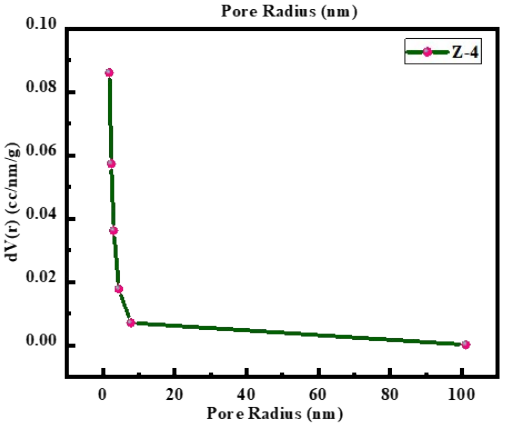
Z-4
dV(r) (cc/nm/g)
Pore Radius (nm)

Fig. S6 (b) Nitrogen adsorption-desorption isotherms and pore size distribution graphs of ZnO samples (Z-1, Z-2, Z-3 and Z-4)

The pore size distribution and SSA of ZnO and surfactant assisted ZnO was further affirmed by N_2 adsorption-desorption isotherms (Fig. S6 (b)). The Fig. S6 (b)depicts the nitrogen adsorption and desorption isotherms, which exhibits the type IV isotherm and pore size distribution curves of the ZnO and surfactant molded ZnO respectively. The type IV isotherms indicate the presence of mesoporous (2-50 nm in pore size) nature of ZnO nanostructures in accord with the IUPAC (International Union of Pure and Applied Chemistry) nomenclature[8,9]. The SSA of all variations of Z-1, Z-2, Z-3, and Z-4 was found to be 181.27 m^2/g, 256.88 m^2/g, 237.41 m^2/g, 215.20 m^2/g, and respectively. The pore size distributions of Z-1, Z-2, Z-3, and Z-4 samples were observed to be 32.64 nm, 17.14 nm, 25.08 nm, and 27.22 nm, respectively. The highest SSA was attributed to the Z-2 sample, CTAB modified ZnO leading to major surface active sites, which results in an increase in the adsorption nature of synthesized material. Prominently, the synthesized ZnO nanostructures have shown SSA which succeeds the synthesized ZnO nanorods to have an optimistic high adsorption capacity of the drug in drug loading and release study, and in the study of bioactivities like antioxidant, antimicrobial and anticancer.

S7. Assessment of antioxidant activity by DPPH scavenging assay

The assessment of the antioxidant activity using DPPH as depicted in Fig. S7 (a).In this study, free radicals have been scavenged by all bioderived carbon samples.In between the carbon samples, C-2 sample demonstrated higher antioxidant activity (60.57 %) as compared to C-4 (52.93 %), C-3 (52.37 %) and C-1 (52.37 %) samples. Also, the hydrothermally synthesized ZnO nanorods implemented superior antioxidant activity as revealed in Fig. S6 (b). The antioxidant activity was found to be 40.12 %.44.54 %, 41.73 %, 43.61 % for Z-1, Z-2, Z-3 and Z-4 samples respectively. Out of these samples, the Z-2 sample overcomes the highest antioxidant activity in comparison with different ZnO series.

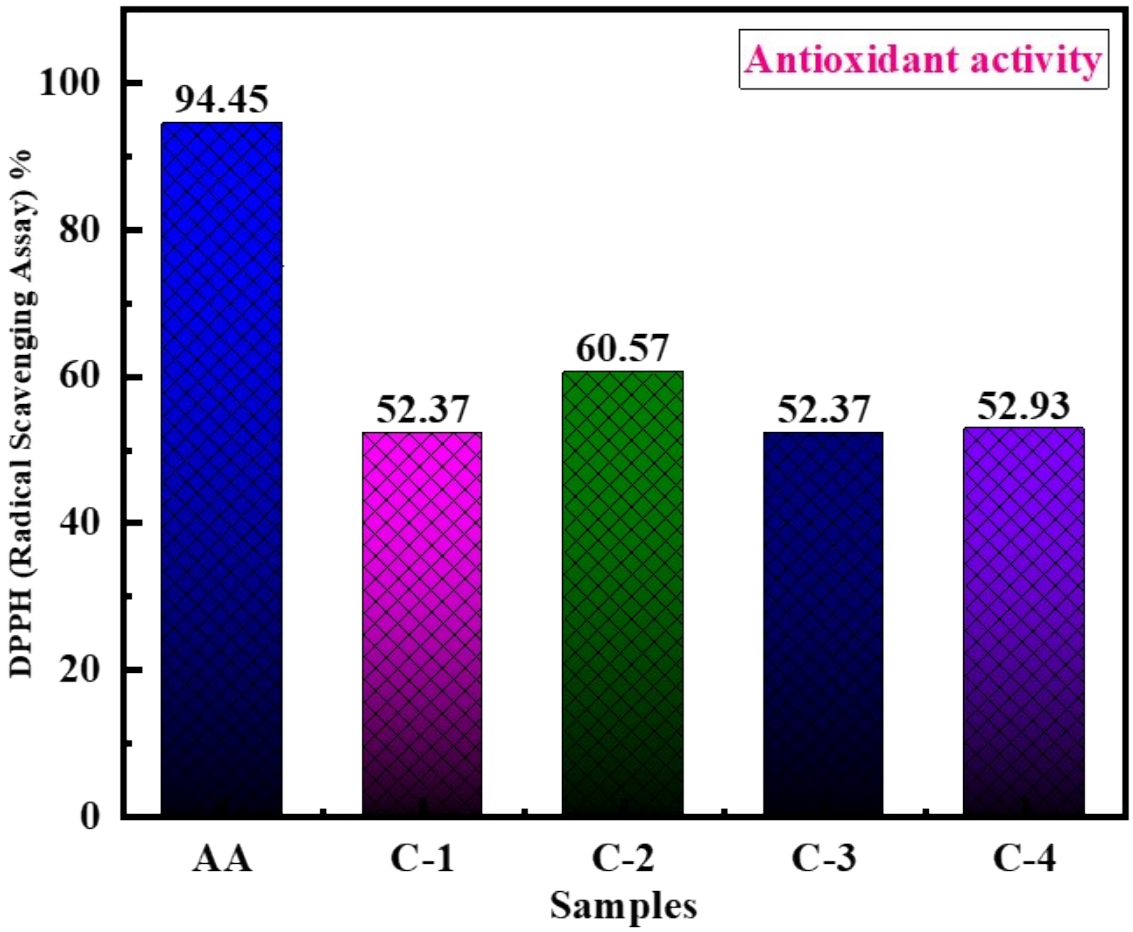

Fig. S7 (a) Antioxidant activity graph of C-1, C-2, C-3 and C-4 samples in comparison with standard ascorbic acid

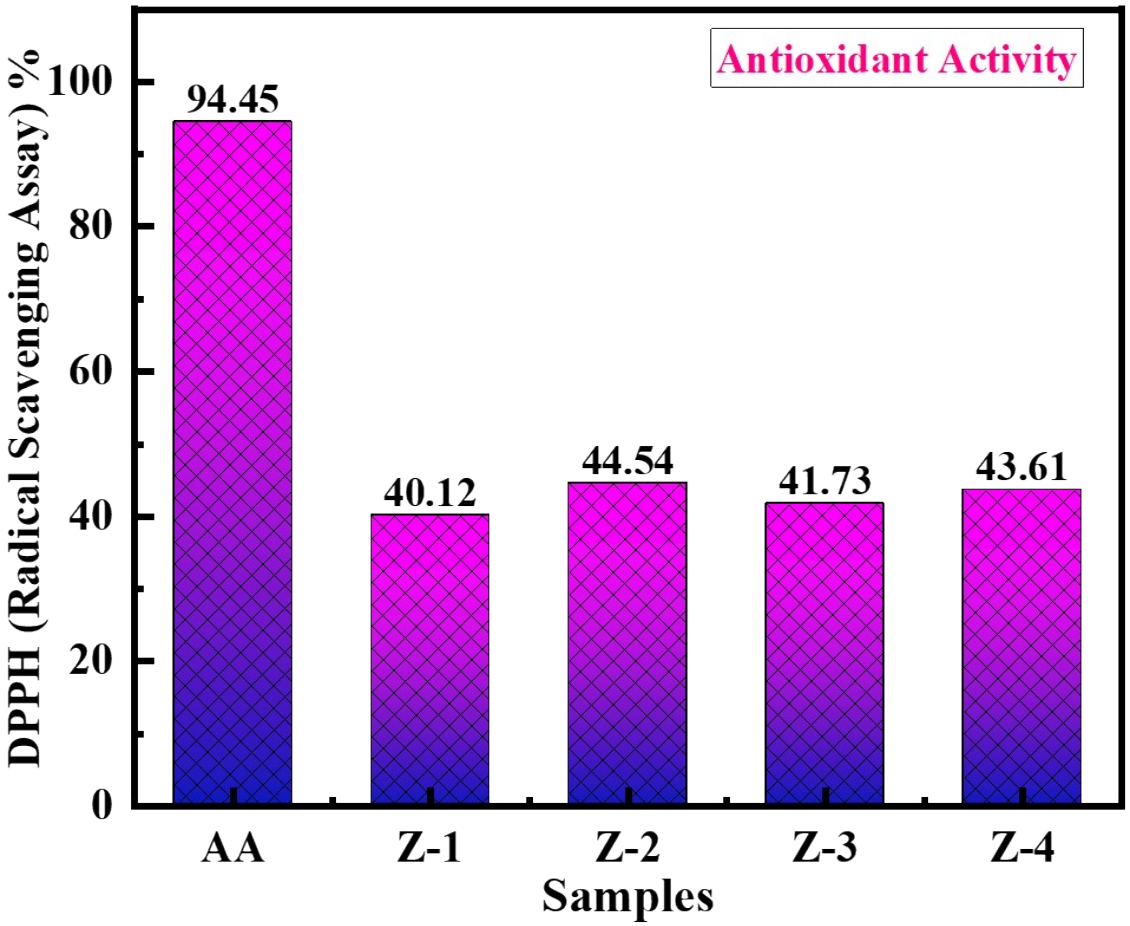

Fig. S7 (b) Antioxidant activity graph of Z-1, Z-2, Z-3, and Z-4 samples in comparison with standard ascorbic acid

S8. Assessment of Anti-microbial activity

The antimicrobial characteristics of synthesizedmesoporous carbon and ZnO samples demonstrated intriguing efficacy against gram-positive and gram-negative pathogens but lack antifungal capabilities as displayed in Fig S8 (a) and (b) respectively. The zone of inhibition of all carbon and ZnO samples against bacterial/fungal species is described in Tables S1 and S2 respectively. Also, the antimicrobial activity of synthesizedmesoporous carbon and ZnO samples as shown in Fig. S8 (c) and Fig. 8 respectively.

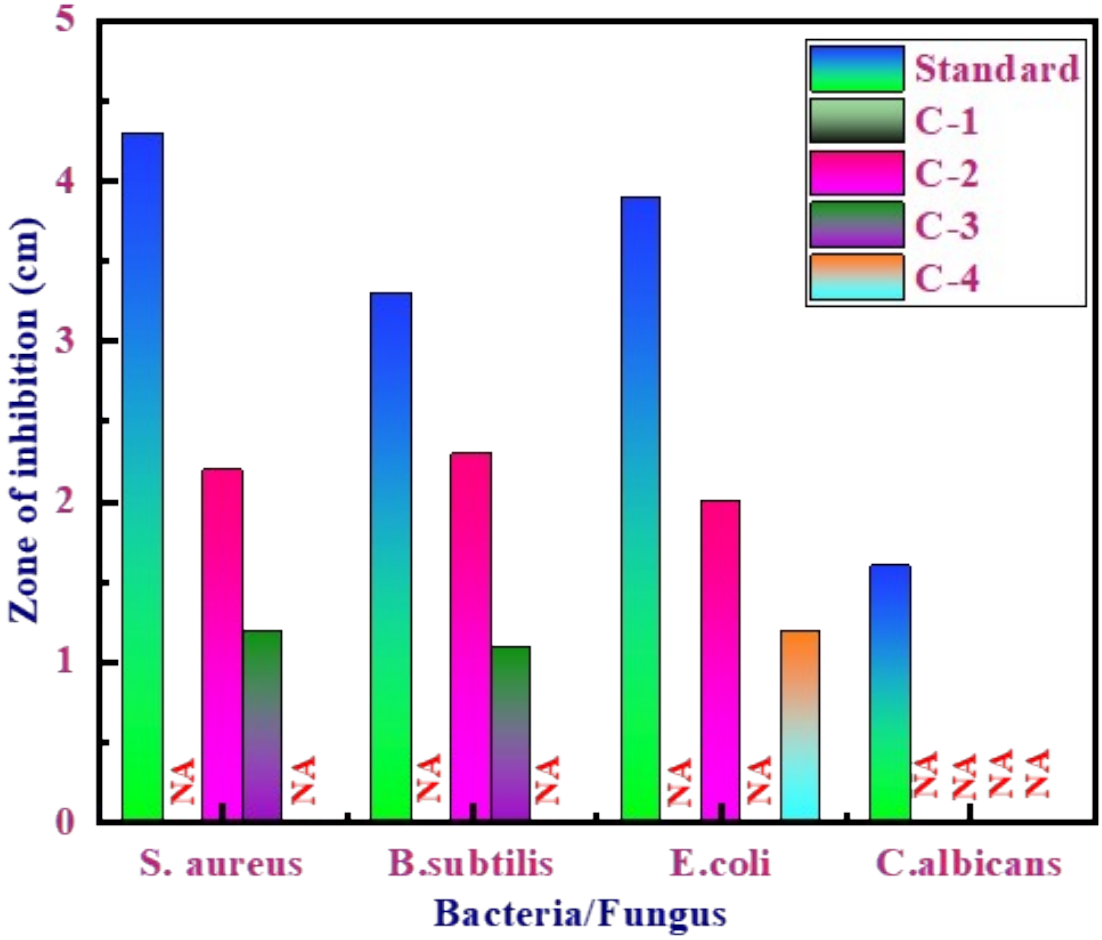

Fig. S8 (a) Inhibitory effect of C-1, C-2, C-3 and C-4 samples by agar well diffusion method on different microbes (zone of inhibition in cm)

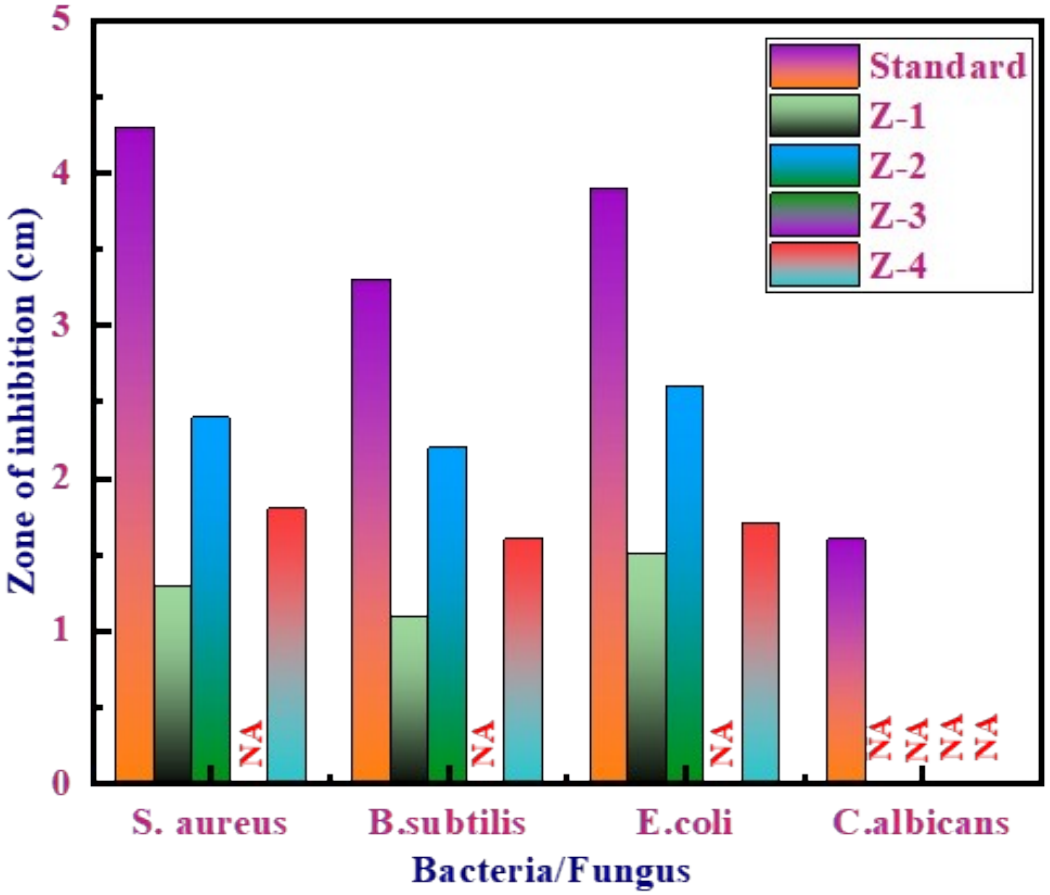

Fig. S8 (b) Inhibitory effect of Z-1, Z-2, Z-3, and Z-4 samples by agar well diffusion method on different microbes (zone of inhibition in cm)

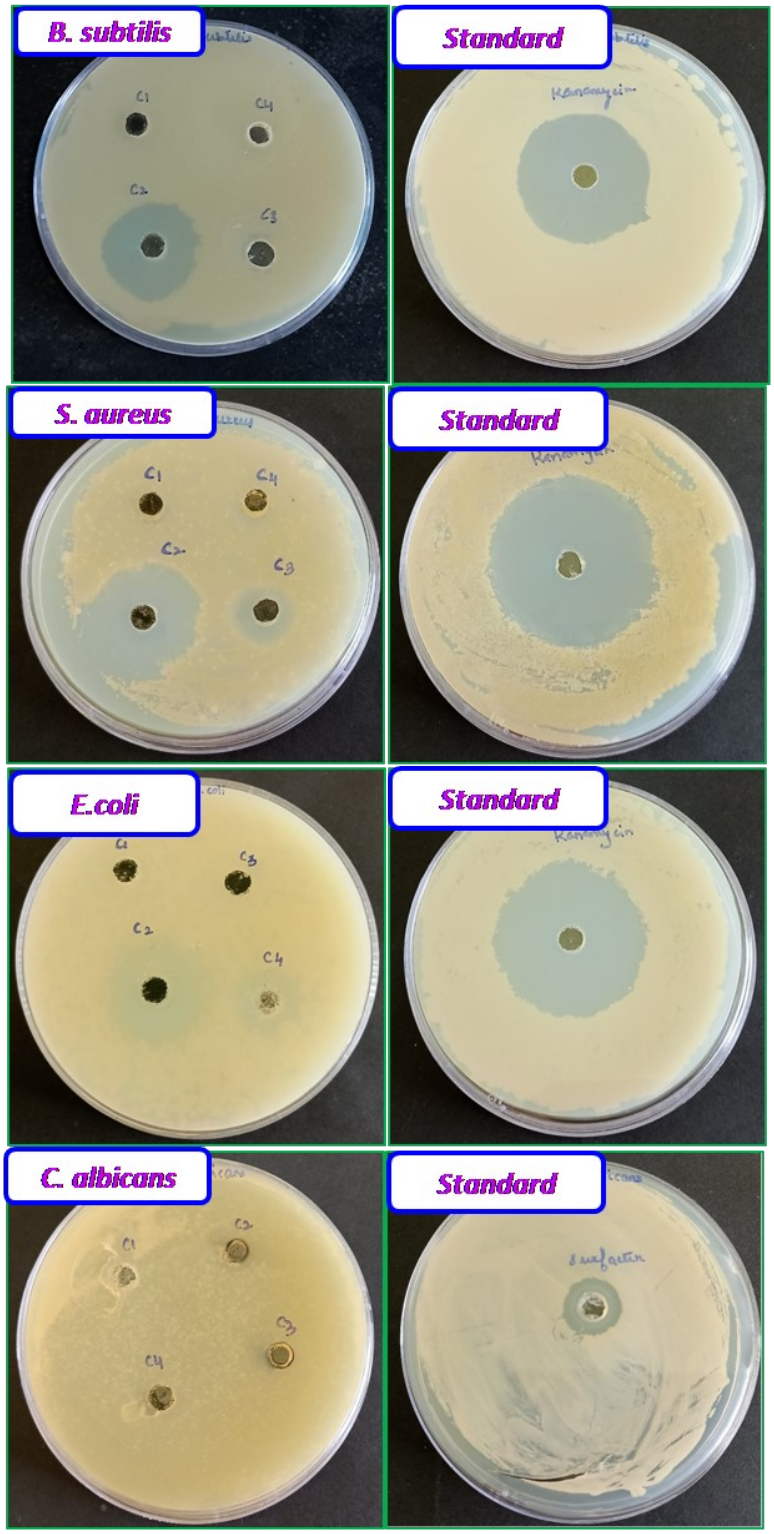

Fig. S8 (c) Standard of all bacterial/fungal species treated against 100 mg of C-1, C-2, C-3 and C-4 samples

S9. EDAX analysis of C-1, C-2, C-3, and C-4 samples

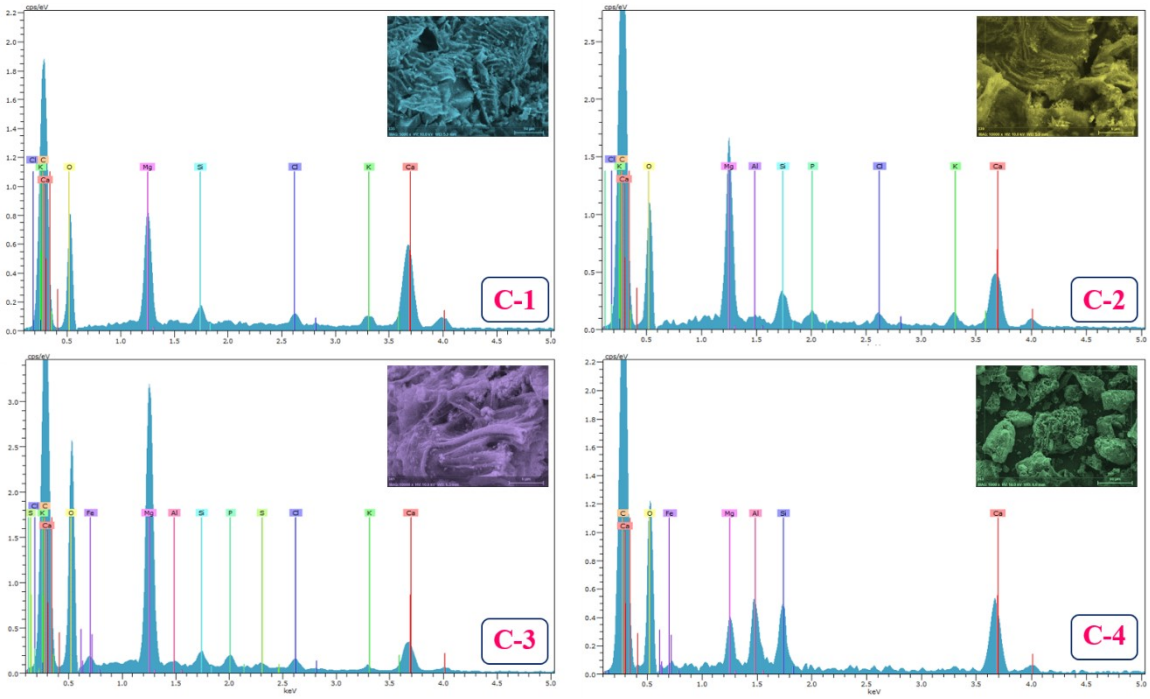

Fig. S9 EDAX spectra of C-1, C-2, C-3 and C-4 samples

We performed EDAX spectra of the C-1, C-2, C-3, and C-4 samples to verify the chemical composition of the samples. The C-1, C-2, C-3, and C-4 samples are not chemically different from one another; instead, they differ in the morphologies that have been modified by surfactants and in other aspects, especially specific surface area, porosity as well adsorption in biomedical applications, etc.

S10. GCMS analysis of *Argyreia sharadchandrajii* biomass

Based on GC-MS analysis, seven compounds from the methanolic extract of *Argyreia sharadchandrajii* were successfully identified **(Table S3).** The compounds were identified based on the retention time, base m/z, molecular weight, peak area, and molecular formula. The most abundant compounds were n- Hexadecanoic acid **(**37.03%**)**, followed by Octadecanoic acid **(**25.08%**)**, Neopytadiene **(**6.69%**)**, Diethyl phthalate **(**4.49%**),** Hexadecanoic acid, methyl ester (2.62%), 1-Nonadecene (1.02%) and one unknown compound (20.16%) **(Supplementary material, GCMS)**. A thorough literature search in online databases such as Web of Science, PubChem, Scopus, and PubMed was conducted to assess the reported biological activity of the identified compounds. Several studies have reported the biological activities of the identified compounds, n-hexadecanoic acids **(5) (Fatty acid)** showed antioxidant, anti-inflammatory, hypocholesterolemic, and nematicide[10,11]. For the first time, K Zahara reported the presence of Octadecenoic acid (Z) **(2) (Natural product)**, methyl ester in the hexane extract of B. bipinnata leaves exhibited antibacterial activity[12]. Neophytadiene **(3) (Natural product)**, which seems to be involved in the antibacterial activity, was found in the *Buxus macowanii* plant extract by GCMS analysis, as stated by B. Ngobeni[13]. Diethyl phthalate **(4) (Phthalate ester)** can be a strong antibacterial agent, according to PREMJANU N[14]. AMUDHA P claimed unique phytocompounds found in *E. acoroides* include 1-nonadecene **(6) (Natural product)**, n-tetracosanol-1, which has antioxidant properties, and triacontane, which has antibacterial, anti-diabetic, and anticancer properties[15].

Table S1: Effect of C-1, C-2, C-3, and C-4 bioderived carbon samples on growth inhibition of bacterial/fungal species

Sr. No.	Name of the bacteria/fungus	Sample code	Zone of inhibition (cm)
1.	*S. aureus*	C-1	NA
		C-2	2.2
		C-3	1.2
		C-4	NA
2.	*B. subtilis*	C-1	NA
		C-2	2.3
		C-3	1.1
		C-4	NA
3.	*E. coli*	C-1	NA
		C-2	2
		C-3	NA
		C-4	1.2
4.	*C. albicans*	C-1	NA
		C-2	NA
		C-3	NA
		C-4	NA

Table S2: Effect of Z-1, Z-2, Z-3, and Z-4 hydrothermally synthesized ZnO samples on growth inhibition of bacterial/fungal species

Sr. No.	Name of the bacteria/fungus	Sample code	Zone of inhibition (cm)
1.	*S. aureus*	Z-1	1.3
		Z-2	2.4
		Z-3	NA
		Z-4	1.8
2.	*B. subtilis*	Z-1	1.2
		Z-2	2.2
		Z-3	NA
		Z-4	1.6
3.	*E. coli*	Z-1	1.2
		Z-2	2.6
		Z-3	NA
		Z-4	1.7
4.	*C. albicans*	Z-1	NA
		Z-2	NA
		Z-3	NA
		Z-4	NA

Table S3: Chemical compounds from the methanolic extract of *Argyreia sharadchandrajii* identified by using the GC-MS technique.

Peak#	R. Time (min)	Phytochemical Compound name	Molecular formula	Base m/z	Area %	Molecular weight
1	35.090	n -Hexadecanoic acid (1)	$C_{16}H_{32}O_2$	73.00	37.03	256
2	38.753	Octadecanoic acid (2)	$C_{18}H_{36}O_2$	57.05	25.08	284
3	32.782	Neophytadiene (3)	$C_{20}H_{38}$	95.10	6.69	278
4	25.644	Diethyl phthalate (4)	$C_{12}H_{14}O_4$	149.00	4.49	222
5	33.756	Hexadecanoic acid, methyl ester (5)	$C_{17}H_{34}O_2$	74.05	2.62	270
6	30.967	1-Nonadecene (6)	$C_{19}H_{38}$	83.10	1.02	266

References

1 S. Feng, Z. Liu, Q. Yu, Z. Zhuang, Q. Chen, S. Fu, L. Zhou and L. Mai, *ACS Appl. Mater. Interfaces*, 2019, **11**, 4011–4016.

2 Z. M. Khoshhesab, M. Sarfaraz and M. A. Asadabad, *Synth. React. Inorganic, Met. Nano-Metal Chem.*, 2011, **41**, 814–819.

3 S. Wang, F. Jia, X. Wang, L. Hu, Y. Sun, G. Yin, T. Zhou, Z. Feng, P. Kumar and B. Liu, *ACS Omega*, 2020, **5**, 5209–5218.

4 S. Talam, S. R. Karumuri and N. Gunnam, *ISRN Nanotechnol.*, 2012, **2012**, 1–6.

5 D. E. Anderson, S. Balapangu, H. N. A. Fleischer, R. A. Viade, F. D. Krampa, P. Kanyong, G. A. Awandare and E. K. Tiburu, *Sensors (Switzerland)*, 2017, **17**, 1–13.

6 C. T. C. Wan, D. López Barreiro, A. Forner-Cuenca, J. W. Barotta, M. J. Hawker, G. Han, H. C. Loh, A. Masic, D. L. Kaplan, Y. M. Chiang, F. R. Brushett, F. J. Martin-Martinez and M. J. Buehler, *ACS Sustain. Chem. Eng.*, 2020, **8**, 9472–9482.

7 T. Chen, M. Li, L. Zhou, X. Ding, D. Lin, T. Duan, G. Yang, R. He and W. Zhu, *ACS Sustain. Chem. Eng.*, 2020, **8**, 6458–6465.

8 M. Y. Nassar, M. M. Moustafa and M. M. Taha, *RSC Adv.*, 2016, **6**, 42180–42195.

9 Y. Feng, N. Feng, Y. Wei and G. Zhang, *RSC Adv.*, 2014, **4**, 7933–7943.

10 R. V. Guerrero, R. A. Vargas and V. L. Petricevich, *Int. J. Pharm. Pharm. Sci.*, 2017, **9**, 42.

11 S. Francis, V. A. Gideon and S. J. Britto, *Int. J. Bot. Stud.*, 2021, **6**, 282–292.

12 K. Zahara, Y. Bibi, M. Arshad, G. Kaukab, S. Al and A. Qayyum, *Saudi J. Biol. Sci.*, 2022, **29**, 472–479.

13 B. Ngobeni, S. S. Mashele, N. J. Malebo, E. Van Der Watt and I. T. Manduna, *BMC Complement. Med. Ther.*, 2020, **20**, 1–8.

14 N. Premjanu and C. Jaynthy, *Asian J. Pharm. Clin. Res.*, 2014, **7**, 141–142.

15 P. Amudha, M. Jayalakshmi, N. Pushpabharathi and V. Vanitha, *Asian J. Pharm. Clin. Res.*, 2018, **11**, 313–317.